Title
Through-plane water distribution in a polymer electrolyte fuel cell: Comparison of numerical prediction with neutron radiography data

Journal
Journal of the Electrochemical Society, 157(12)

ISSN
0013-4651

Authors
Wang, Y
Chen, KS

Publication Date
2010-11-24

DOI
10.1149/1.3498997

Peer reviewed

Journal of The Electrochemical Society, **157** (12) B1878-B1886 (2010)
0013-4651/2010/157(12)/B1878/9/$28.00 © The Electrochemical Society

Through-Plane Water Distribution in a Polymer Electrolyte Fuel Cell: Comparison of Numerical Prediction with Neutron Radiography Data

Yun Wang[a,*,z] **and Ken S. Chen**[b,*]

[a]*Renewable Energy Resources Lab and National Fuel Cell Research Center, Department of Mechanical and Aerospace Engineering, The University of California, Irvine, Irvine, California 92697-3975, USA*
[b]*Engineering Sciences Center, Sandia National Laboratories, Albuquerque, New Mexico 87185, USA*

A multidimensional mathematical model is presented for simulating the coupled phenomena of gaseous fuel/reactant flows, species (including liquid water) transport, heat transfer, hydrogen oxidation, and oxygen reduction reactions in a polymer electrolyte fuel cell (PEFC). The present work focuses on elucidating water distribution in the through-plane direction, in particular across the membrane electrode assembly (MEA) and gas diffusion layer (GDL). Two-dimensional model predictions are computed numerically and compared with available experimental data from neutron radiography or imaging. Using the same set of model parameters, reasonably good agreements are obtained quantitatively between the computed water profile in the MEA–GDL component and the neutron-imaging data reported by two separate research groups, and qualitatively between model prediction and the data from another (third) group. Case-study simulations are carried out for PEFC operation at various temperatures, relative humidities, and current densities. It is found that liquid-water content is lower at higher cell temperatures due to greater water evaporation and stronger water diffusion in the vapor phase, as expected. Without strong water diffusion in the vapor phase, the liquid-water profiles are found to increase with current density in the cathode GDL but indicate a complex trend in the anode. Effect of varying GDL thermal conductivity on water distribution is also examined.
 [DOI: 10.1149/1.3498997]

Manuscript submitted January 21, 2010; revised manuscript received September 14, 2010. Published October 27, 2010.

Polymer electrolyte fuel cells (PEFCs) have been receiving a great deal of attention in the scientific research community recently due to their potential to reduce our petroleum-based energy use and pollutant emissions associated with petroleum-based energy generation. Phenomena involved in a PEFC are complex and encompass the fundamentals of heat transfer, species transport, multiphase flows, and electrochemical reactions. Multiphase flow originates from water production by the oxygen reduction reaction (ORR) in the cathode of a PEFC. When the local water vapor partial pressure reaches its saturation value, condensation occurs and liquid emerges, leading to the co-existence of gas and liquid and resultant two-phase flow (see Fig. 1). Liquid water must be efficiently removed from the reaction sites in the catalyst layer (CL) where the ORR takes place, through the gas diffusion layer (GDL), and eventually out of the flow channels of a PEFC in order to avoid its adverse impact on the oxygen-reactant supply and thus sustain the electrochemical energy conversion.

Numerous PEFC modeling activities have been conducted by many groups. Two comprehensive reviews on the PEFC modeling work were recently provided by Wang[1] and Weber and Newman,[2] respectively. Early studies primarily focused on the PEFC phenomena in reduced dimensions (e.g., 1D models by Springer et al.,[3] Bernardi and Verbrugge,[4] and Rowe and Li,[5] and 2D models by Nguyen and White,[6] Gurau et al.,[7] and Um et al.[8]) and most of them excluded the presence of liquid water and its transport. Early PEFC models incorporating liquid-water transport were presented by several research groups.[9-12] These pioneering efforts provided a framework for the subsequent more complex models that consider full three dimensions, additional physics, or more detailed characteristics of PEFC components. Among these subsequent models, authors in Ref. 13-18 reported isothermal fuel cell models and they investigated the two-phase transport and impacts without considering temperature variation. Nonisothermal condition was included by authors in Ref. 19-25, who explored the interaction between heat transfer and liquid transport. A new mechanism for water/heat transport similar to the heat pipe effect was identified.[24,25] Luo et al.[26] and Wang[27] extended the two-phase flow from the cathode to the anode and found that flooding may appear under the anode land even at low humidity operation. These authors further expanded their model capabilities to capture the single-/two-phase transition in the diffusion media, which requires advanced numerical schemes to describe the sharp interface. Two-phase flow in PEFC reactant channel was analyzed and the importance of the channel liquid flow on reactant delivery was addressed in several studies.[2,28] Nam and Kaviany[19] and Wang et al.[30] investigated the impacts of GDL characteristics (e.g., carbon paper versus carbon cloth, media tortuosity, and carbon fiber properties) on species transport, water flow, and PEFC performance. Very recent studies were carried out by Basu et al.[31] on the phase change (water vapor condensation, liquid-water evaporation). Lastly, pore-scale species and charge transport through the cathode catalyst layer were modeled via direct numerical simulation by Mukherjee and Wang[32] and the mesoscopic modeling of two-phase behaviors in a PEFC was carried out by Mukherjee et al.[33]

Though great progress has been made on modeling PEFCs and some comparisons between model predictions and experimental data have been reported,[27,28,30,34-36] more model validation is needed, in particular in the two-phase operating regime in which liquid water is present. The lack of such direct comparisons is partly due to the great difficulty in probing the in situ liquid-water profile within an operating PEFC, particularly the through-plane water profiles because most PEFC components are very thin at the microscale. The through-plane profiles are extremely helpful in understanding the transport characteristics across the membrane electrode assembly (MEA), GDL, and channel. Many neutron imaging studies aiming at probing liquid-water distribution within the active areas of an operating PEFC have been reported in the open literature[37-42] but the through-plane water profiles obtained via neutron imaging were obtained only until recently when the high-resolution neutron radiography became available.[43-46] In Hickner et al.'s high-resolution neutron imaging work,[44] the through-plane water profiles were measured, using a pixel size of ~ 15 μm, across the MEA–GDL in wide ranges of temperatures and current densities. In addition, Hickner et al.'s pioneering high-resolution neutron experiments provided the direct evidence for the anode flooding. Following Hickner et al.'s work, quantitative through-plane water content profiles obtained by neutron imaging were also reported by the fuel cell research group at Las Alamos National Laboratory (LANL).[45,46] In addition to neutron radiography, other techniques such as magnetic resonance imaging[47] and X-ray imaging[48] have also been employed to probe liquid-water content in PEFCs.

A direct comparison between the predicted water through-plane profiles and neutron imaging data was attempted recently by Weber

* Electrochemical Society Active Member.
z E-mail: yunw@uci.edu

and Hickner.[36] Their model prediction agrees reasonably well for the 80°C case (though no liquid is shown in the anode), but a 300% discrepancy or factor of 4 difference[46] exists for the 60°C case. Weber and Hickner attributed the large discrepancy to their pseudo two-dimensional (2D) (or 1 + 1D) approach in which the ribs are neglected; and they pointed out that model improvement is needed for an accurate prediction, e.g., a more refined and validated membrane model and a full 2D model including rib/channel effects are needed. Reference 24 also demonstrated that the in-plane direction is also important for the water vapor diffusion and heat pipe process. The present work sought to elucidate the water through-plane profiles by developing a full 2D PEFC model to account for both rib and channel effects and incorporate a detailed MEA model. Model validation was performed by direct comparisons of the computed water through-plane profiles with the neutron-imaging data from Hickner et al.[44] of Sandia National Laboratories and Mukundan and Borup[45] and Borup[46] of LANL. The validated model was then applied to elucidate the effects of current density, relative humidity (RH), and temperature on water distribution and PEFC performance. Effect of varying GDL thermal conductivity was also examined. It should be noted, this paper is not intended to focus on modeling new phenomena. Rather, we make one of the first attempts to address an important issue of comparing the prediction from a fuel cell model with the neutron imaging data in terms of water through-plane distribution.

Mathematical Model

Governing equations.— In the present paper, we consider the electrochemical and transport phenomena in the key components of a PEFC, namely, the MEA consisted of the catalyst layers and membrane, GDLs, gas flow channels, and bipolar plates. Two-phase transport is modeled in the regions of the CLs, membrane, and GDLs. Since the current mathematical treatment for the microporous layer (MPL) region, as demonstrated by Weber and Hickner's model predictions, appears unable to describe the smooth water-content transition at the MPL–GDL interfaces (which was observed in experiments), we decided not to explicitly model the MPL in the present work; rather, we account for the MPL effect by adjusting CL properties. Note that it is possible that MPLs extend into the GDL pore space which leads to the smooth transition. However, to our knowledge no experimental studies have been conducted to quantify the extension (e.g., what degree of the extension exists and how properties change in the transition) and modeling the extension has not been well developed. In addition, detailed electrochemical reactions (hydrogen oxidation reaction or HOR in the anode and ORR in the cathode) within the catalyst layers are included. The membrane swelling is also excluded in the present work as its impacts are not yet fully understood and no validated models have been developed. We also model the heat and electron transport in the graphite bipolar plates. The governing equations are based on the conservations of mass, momentum, species, charges, and energy, and can be presented in a general form as follows

$$\text{Continuity equation:} \quad \nabla \cdot (\rho \vec{u}) = 0 \tag{1}$$

$$\text{Momentum conservation:} \quad \frac{1}{\varepsilon^2} \nabla \cdot (\rho \vec{u}\vec{u}) = -\nabla P + \nabla \cdot \rho\tau + S_u \tag{2}$$

$$\text{Energy conservation:} \quad \nabla \cdot (\gamma_T \rho c_p \vec{u} T) = \nabla \cdot (k^{\text{eff}} \nabla T) + S_T \tag{3}$$

$$\text{Reactant species conservation:} \quad \nabla \cdot (\gamma_k \vec{u} C_k) = -\nabla \cdot \vec{G}_{k,\text{diff}} + S_k \tag{4}$$

$$\text{Water conservation:} \quad \nabla \cdot (\gamma_w \vec{u} C_w) = -\nabla \cdot (\vec{G}_{w,\text{diff}} + \vec{G}_{w,\text{perm}}) - \nabla \cdot \left[\left(\frac{m f_l^k}{M^k} - \frac{C_g^k}{\rho_g} \right) \vec{j}_l \right] + S_w \tag{5}$$

Table I. Source terms of several conservation equations.[1,24,27]

	S_u	S_{C_k}	S_{C_w}	$S_{\Phi^{(m)}}/S_{\Phi^{(s)}}$
Bipolar plates	-	-	-	-/0
Gas channels	$-\nabla P$	0	0	-
GDL	$-\frac{\mu}{K_{GDL}}\vec{u}$	0	0	-/-
Anode catalyst layer	$-\frac{\mu}{K_{CL}}\vec{u}$	$-\frac{j}{2F}$	0	$j/-j$
Cathode catalyst layer	$-\frac{\mu}{K_{CL}}\vec{u}$	$\frac{j}{4F}$	$-\frac{j}{2F}$	$j/-j$
Membrane	-	0	0	0/-

$$\text{Charge conservation (protons):} \quad 0 = \nabla \cdot (\sigma_m^{\text{eff}} \nabla \Phi^{(m)}) + S_{\Phi^{(m)}} \tag{6}$$

$$\text{Charge conservation (electrons):} \quad 0 = \nabla \cdot (\sigma_s^{\text{eff}} \nabla \Phi^{(s)}) + S_{\Phi^{(s)}} \tag{7}$$

where ρ the multiphase mixture density, $\vec{u}$ the superficial fluid velocity vector, p the pressure, C_k/C_w the molar concentration of reactant/water, T the temperature, $\Phi^{(m)}/\Phi^{(s)}$ the electronic/electrolyte phase potentials. $\vec{G}_{\text{diff}}$ includes the diffusion fluxes in gaseous, liquid, and solid electrolyte phases. $\vec{G}_{w,\text{perm}}$ represents the hydraulic permeation water flux through the membrane. The electrochemical and transport processes are coupled together through the model parameters and source terms. Table I lists the expressions for several sources terms. Details of the parameters and source terms can be found in Ref. 24 and 27. The key aspects regarding the model and electrochemical/transport phenomena that are closely related to the topic of this paper are elaborated below.

Electrochemical kinetics.— The electrochemical reactions take place within the catalyst layers as follows

$$\text{HOR in the anode:} \quad H_2 \rightarrow 2H^+ + 2e^- \tag{8}$$

$$\text{ORR in the cathode:} \quad O_2 + 4e^- + 4H^+ \rightarrow 2H_2O \tag{9}$$

The Butler–Volmer equation is customarily adopted to describe the electrochemical reaction rate

$$j = a i_0 \left\{ \exp\left(\frac{\alpha_a}{RT} F \cdot \eta \right) - \exp\left(-\frac{\alpha_c}{RT} \cdot F \cdot \eta \right) \right\} \tag{10}$$

where the surface-to-volume ratio a evaluates the roughness of porous electrodes. The presence of liquid water in the catalyst layer may reduce the reaction area as follows

$$a = (1 - s)^{\tau_a} a_0 \tag{11}$$

where the liquid-water saturation s is defined as the volume fraction of liquid water in the void space.

In PEFCs, HOR is fast, thus yielding a relatively small anode overpotential. Therefore, Eq. 10 for the anode can be adequately simplified to a linear kinetic equation. For ORR, sluggish kinetics results in a large cathode overpotential. Consequently, the Butler–Volmer equation can be approximated by the Tafel kinetics. In addition, the reaction rate of the ORR highly depends on temperature as described by the Arrhenius expression. The HOR and ORR kinetic rate expressions are thus simplified to the following

$$\text{anode:} \quad j_a = a i_{0,a}^{\text{ref}} \left(\frac{C_{\text{H2}}}{C_{\text{H2}}^{\text{ref}}} \right)^{1/2} \left(\frac{\alpha_a + \alpha_c}{RT} \cdot F \cdot \eta \right) \tag{12}$$

$$\text{cathode:}\quad j_c = -ai_{0,c}^{\text{ref}} \exp\left[-\frac{E_a}{R}\left(\frac{1}{T}-\frac{1}{353.15}\right)\right]\left(\frac{C_{O2}}{C_{O2}^{\text{ref}}}\right) \times\exp\left(-\frac{\alpha_c F}{RT}\cdot\eta\right) \quad [13]$$

where E_a denotes the activation energy for ORR at the Pt/Nafion electrode and the surface overpotential is defined as

$$\eta = \Phi^{(s)} - \Phi^{(m)} - U_o \quad [14]$$

The equilibrium potential U_o is a function of temperature.[1,24,27]

Two-phase transport in porous media.— Two-phase transport in PEFCs originates from water production by the ORR. In a PEFC, both the GDL and catalyst layer are highly porous media, allowing heat and species transport. Liquid may emerge in the pore when the water vapor partial pressure reaches its saturation pressure, resulting in two-phase flow. The two-phase mixture density is defined as[49]

$$\rho = s\rho^{(l)} + (1-s)\rho^{(g)} \quad [15]$$

The saturation s can be obtained from the mixture water concentration C_w

$$s = \begin{cases} 0, & C_w \leqslant C_{\text{sat}} \\ \dfrac{C_w - C_{\text{sat}}}{\rho^{(l)}/M_w - C_{\text{sat}}}, & C_w > C_{\text{sat}} \end{cases} \quad [16]$$

One major interaction between the two-phase flows is described through the relative permeabilities $k_r^{(l)}$ and $k_r^{(g)}$, defined as the ratio of the intrinsic permeability of liquid and gas phases, respectively, to the total intrinsic permeability of a porous medium. Physically, these parameters describe the extent to which one fluid is hindered by others in pore spaces, and hence can be formulated as a function of liquid saturation. One formula for the relative permeabilities is as follows

$$k_r^{(l)} = s^3 \quad \text{and} \quad k_r^{(g)} = (1-s)^3 \quad [17]$$

In addition, residual liquid may be present as observed by Hickner et al.,[44] who probed the through-plane distribution of residual water at vanishing current. Modeling residual liquid impact has been attempted by several studies.[29,50-52] In the present work, we exclude the residual water due to the following two considerations: (1) there are no accurate/validated models on residual water for the carbon-fiber-based GDL in PEFCs; and (2) the data of in situ residual water are not available for cases with various currents which will be used for model validation. Without the direct data from the in situ experiment, adding residual water (and its spatial distribution) becomes arbitrary and may be unsuitable to be used for elucidating the water profile in an operating fuel cell.

Fuel, oxidant, and water transport.— In the gaseous phase, hydrogen, oxygen, and water follow similar transport mechanisms. Modeling their transport can be found in our previous paper,[27] therefore not repeated here. To account for the liquid impact, we modify the effective diffusivity by

$$D^{(g),\text{eff}} = [\varepsilon(1-s)]^{\tau_d} D^{(g)} \quad [18]$$

The convection corrector factor γ is a function of s

$$\gamma_k = \frac{\rho\lambda^{(g)}}{\rho^{(g)}(1-s)} \quad \text{and} \quad \gamma_w = \frac{\rho}{C_w}\left(\frac{\lambda^{(l)}}{M_w} + \frac{\lambda^{(g)}}{\rho^{(g)}}C_{\text{sat}}\right) \quad [19]$$

where $\lambda^{(l/g)}$ the relative mobilities of individual phases. The capillary pressure P_c, which may be the primarily driving force for liquid-water transport, is given as follows

$$P^{(g)} - P^{(l)} = P_c = \sigma\cos(\theta_c)\left(\frac{\varepsilon}{K}\right)^{1/2} J(s) \quad [20]$$

where σ is the surface tension. $J(s)$ for the hydrophobic diffusion media considered in the present work is given by[27]

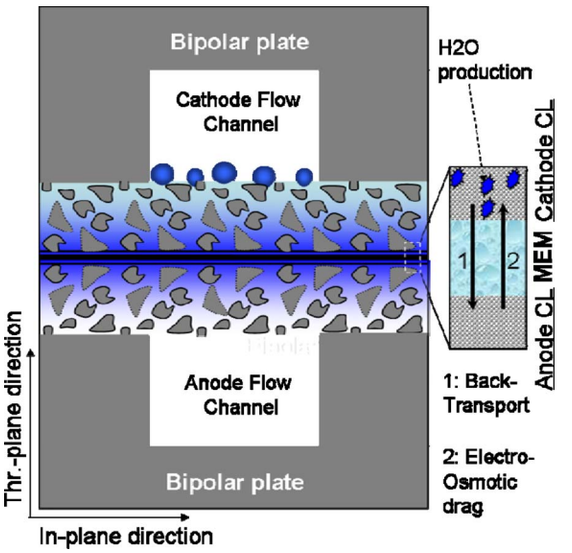

Figure 1. (Color online) The schematic of water in a PEFC.

$$J(s) = 1.417s - 2.120s^2 + 1.263s^3 \quad [21]$$

Once the capillary pressure is calculated, the flux $\vec{j}^{(l)}$ in the water equation of Eq. 5 can be obtained through

$$\vec{j}^{(l)} = \frac{\lambda^{(l)}\lambda^{(g)}}{\nu} K[\nabla P_c + (\rho^{(l)} - \rho^{(g)})\vec{g}] \quad [22]$$

Water transport in the Nafion membrane.— Water in the Nafion membrane is bonded with the sulfonic acid groups in the ionomer. The water content λ is typically adopted to characterize the membrane hydration level and defined as the number of water molecules per sulfonic group. It is related to the equivalent water concentration through the following equation

$$C_w^{(m)} = \alpha\frac{\rho^{(m)}\lambda}{EW} \quad [23]$$

where $\rho^{(m)}$ and EW are the density and equivalent molecular weight of the membrane, respectively. In the above equation, we use α to account for several factors that may affect the water content within the membrane, such as membrane swelling due to hydration by water (which reduces the membrane density), compression due to load or force applied at the external wall surfaces (which results in less water than one would expect theoretically), and incomplete dissociation of proton. Two processes may shape the membrane water content profile: one is the water electro-osmotic drag, the other is water back transport including diffusion and hydraulic permeation (see Fig. 1). The coefficient of the electro-osmotic drag n_d depends on the local water content[53]

$$n_d = \begin{cases} 1.0 & \text{for} \quad \lambda \leqslant 14 \\ \dfrac{1.5}{8}(\lambda - 14) + 1.0 & \text{otherwise} \end{cases} \quad [24]$$

The water diffusion coefficient in the membrane is also a function of water content and the diffusive flux is given by

$$\vec{G}_{w,\text{diff}} = -D_w^{(m)} \nabla C_w^{(m)} \quad [25]$$

where[54]

$$D_w^{(m)} = \begin{cases} 3.1\times10^{-3}\lambda(e^{0.28\lambda} - 1)\cdot e^{[-2436/T]} & \text{for } 0 < \lambda \leqslant 3 \\ 4.17\times10^{-4}\lambda(1 + 161e^{-\lambda})\cdot e^{[-2436/T]} & \text{otherwise} \end{cases} \quad [26]$$

As to the catalyst layers or Gore™ membranes, the diffusivity in the portion of the ionomer is modified by

$$D_w^{(m),\text{eff}} = \varepsilon_m^{\tau_m} D_w^{(m)} \quad [27]$$

Assuming local microscopic thermodynamic equilibrium between ionomer and surrounding fluid, one can combine the diffusive transport in the void space and ionomer by defining an effective diffusion coefficient

$$D_w^{\text{eff}} = \varepsilon^{\tau_d} D_w^{(g)} + \varepsilon_m^{\tau_m} \frac{\rho^{(m)}}{EW} \frac{RT}{P_{\text{sat}}} \frac{d\lambda}{da} D_w^{(m)} \quad [28]$$

where $\rho^{(m)}$ is the density of a dry membrane and the membrane water content is calculated following Spring et al.,[3] Luo et al.,[26] and Wang[27]

$$\lambda = \begin{cases} 0.043 + 17.81a - 39.85a^2 + 36.0a^3 & \text{for } 0 < a \leqslant 1 \\ 14 + 8s & \text{for } 0 < s \leqslant 1 \end{cases}$$

$$a = \frac{C_w}{C_{\text{sat}}} \quad \text{and} \quad C_{\text{sat}}(T) = \frac{P_{\text{sat}}(T)}{RT}, \text{ where}$$

$$\log_{10} P_{\text{sat}} = -2.1794 + 0.02953(T - 273.15) - 9.1837 \times 10^{-5}(T - 273.15)^2 + 1.4454 \times 10^{-7}(T - 273.15)^3 \quad [29]$$

In addition to diffusion, hydraulic permeation may be another mechanism for water transport in the membrane. The permeation flux is determined by the membrane permeability K_m and liquid pressures[27]

$$\vec{G}_{w,\text{perm}} = -\frac{K_m}{M_w \nu^{(l)}} \nabla P^{(l)} \quad [30]$$

Here, we assume liquid-water pressure in the membrane is linear in the through-plane direction, determined by the difference of $P^{(l)}$ s at the membrane surface.

Heat transfer.— Fuel cell produces waste heat during its operation. The major heat generation mechanisms are the reversible/irreversible electrochemical processes, Ohmic resistance, and phase change. The source term S_T in the energy equation can be generalized by

$$S_T = j\left(\eta + T\frac{dU_o}{dT}\right) + \frac{i^{(m)^2}}{\sigma_m^{\text{eff}}} + \frac{i^{(s)^2}}{\sigma_s^{\text{eff}}} + S_{fg} \quad [31]$$

where S_{fg} represents the heat release/absorption due to water condensation/evaporation and the associated phase change rate can be calculated through the water two-phase transport equation. Note that some terms in Eq. 31 may vanish in some fuel cell components, e.g., in the anode GDL there is no ionic currents, therefore the second term on the right disappears. In the bipolar plates, only the third term on the right is nonzero in the above thermal source.

Boundary conditions.— Equations 1-7 form a complete set of governing equations with eight unknowns: $\vec{u}$ (with three components), P, C_k, C_w, T, $\Phi^{(m)}$, and $\Phi^{(s)}$. Their corresponding boundary conditions are briefly described as follows:

Flow inlet boundaries: The inlet velocity $\vec{u}_{in}$ in a gas channel is expressed by the respective anode or cathode stoichiometric flow ratio, i.e., ξ_a or ξ_c, defined at the average current density I as

$$\begin{pmatrix} \vec{u}_{in,a} \\ \vec{u}_{in,c} \end{pmatrix} \cdot \vec{n}\Big|_{\text{inlet}} = -\frac{IA_m}{F} \left(\begin{array}{c} \dfrac{\xi_a}{2C_{\text{H2}}A_a} \\ \dfrac{\xi_c}{4C_{\text{O2}}A_c} \end{array} \right)\Bigg|_{\text{inlet}} \quad [32]$$

where A_a, A_c, and A_m are the flow cross-sectional areas of the anode and cathode gas channels and the membrane, respectively. The inlet molar concentrations are determined by the inlet pressure and humidity according to the ideal gas law.

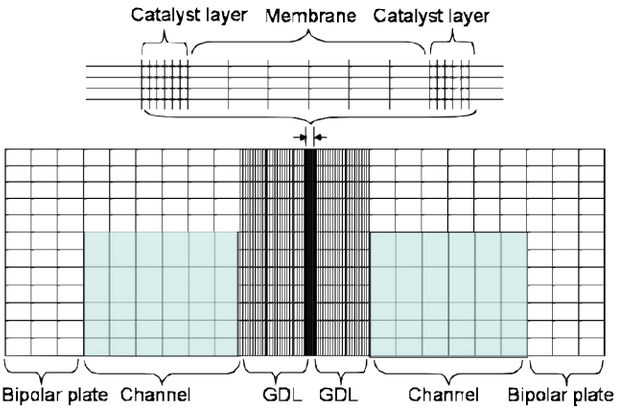

Figure 2. (Color online) The computational domain of the 2D PEFC.

Outlet boundaries.— Fully developed or no-flux conditions are applied.

Walls.— No-slip and impermeable velocity condition and no-flux condition are imposed for the mass, momentum, proton, and species conservation equations. The boundary conditions for the electronic phase potential $\Phi^{(s)}$ and temperature T at the bipolar plate outer surfaces can be expressed as

$$\frac{\partial \Phi^{(s)}}{\partial n}\Big|_{\text{cathode}} = -\frac{IA_m}{\sigma^{\text{eff}} A_{c,\text{wall}}}; \quad \Phi^{(s)}|_{\text{anode}} = 0; \quad T|_{\text{anode/cathode}} = T_{\text{cell}} \quad [33]$$

where $A_{c,\text{wall}}$ is the area of the cathode outer surface. At other wall surfaces, symmetry conditions are applied for these two variables. Further details can be found in Ref. 27.

Numerical Procedures

The governing equations, Eq. 1-7, along with its boundary conditions are discretized by the finite volume method and solved in the commercial CFD software package, Fluent (version 6.0.12), by SIMPLE (semi-implicit pressure linked equation) algorithm. The SIMPLE algorithm updates the pressure and velocity fields from the solution of a pressure correction equation, solved by algebraic multigrid method. Following the solution of the flow field, the energy, species, proton, and electron equations are solved. The source terms and physical properties are implemented in a user-defined function and the species/charge transport equations are solved through the software's user-defined scalars. The mesh of a single-channel 2D PEFC employed for the numerical study is shown in Fig. 2. Totally ~50 gridpoints are adopted in the through-direction for the GDLs (both anode and cathode) to precisely capture the through-plane liquid transport. Twelve gridpoints are employed to capture transport in the fuel cell land-channel structure. The geometrical and operating parameters are listed in Table II. In all the simulations to be presented in the next section, the converged values of species imbalance (i.e., H_2, O_2, and H_2O) are all less than 1% and equation residuals are smaller than 10^{-6}.

Results and Discussion

The water saturation and temperature distributions in both anode and cathode GDLs for three operating temperatures and the current density of 0.75 A/cm^2 are displayed in Fig. 3 and 4. From the water-content (in terms of liquid saturation) contours in Fig. 3, it can be seen that part of the cathode GDL is free of liquid water for the 80°C case, whereas it is fully wetted for the other two cases (60 and

Table II. Geometrical, physical, and operating parameters.

Quantity	Value
Channel depth/width and land width	1.0/1.5 and 1.0 mm
Catalyst layer/membrane thickness	0.01/0.052 mm
Anode/cathode GDL thickness	0.406/0.34 mm
Anode/cathode pressures, P	2.2/2.2 atm
Porosity of GDLs/catalyst layers, ε	0.7/0.5
Humidification in the anode and cathode	100/100%
Water concentration correction factor, α	0.15
Volume fraction of ionomer in catalyst layers, ε_m	0.2
Electronic conductivity of GDLs/bipolar plates, σ_s^{eff}	500/2000 W m^{-1} K^{-1}
Viscosity of liquid water, $\mu^{(l)}$	3.5×10^{-4} kg/m s
Permeability of GDL/membrane, K_{GDL}/K_m	$10^{-12}/5 \times 10^{-20}$ m^2
Surface tension, liquid-water-air (80°C), σ	0.0625 N/m
Thermal conductivity of the membrane/catalyst layer/GDL/bipolar plate	0.95/3.0/3.0/20.0 W/m K
Contact angle of the GDL, θ_c	120°
Exchange current density × reaction surface area, $a_0 i_{0,a}/a_0 i_{0,c}$	$1.0 \times 10^9/0.5 \times 10^4$ A m^{-3}

40°C). This can be explained by the water-vapor-phase diffusion, which is stronger at a higher operating temperature and may be comparable with water production rate.[24] This mechanism drives water vapor from the region under the channel to that under the land, thus enhancing the local saturation under the land at higher operating temperature. This explanation can also be applied to describe the trend in the anode: part of the GDL is in single-phase region for all the cases, and the two-phase region enlarges with lowering operating temperature. In addition, these figures indicate that a very fine mesh (which is made feasible in a 2D geometry across the MEAs and GDLs) and 2D geometry are necessary to capture the through/in-plane water distribution due to the very distinct water profiles in the regions under the channel and land, respectively.

The temperature contours in the three cases (40, 60, and 80°C) look similar but differ in magnitude as shown in Fig. 4. The temperature gradients can be observed in two major directions: one from the region under the channel to that under the land, the other from the catalyst layer to the land. It is important to note that the temperature gradient is the driving force for the water vapor diffusion in the two-phase region. In addition, at a lower temperature operating condition, the temperature variation is slightly higher, which is due to the larger voltage loss arising from the irreversible process.

Figure 5 shows the distributions of the water content in the membrane for the three cases. It can be seen that the water-content contours in the 80°C case is quite different from those in the other two cases: the under-channel membrane region has a lower water content at 80°C. This can be explained with the aid of the water distributions in the anode in the previous figures where at 80°C a large under-channel area in the anode side is dry or free of liquid. For the 40 and 60°C cases, the contours are similar to each other.

In Fig. 6, the through-plane water profiles computed from the present 2D simulation are compared with the neutron-imaging data from Hickner et al.[44] at three operating temperatures. Agreement between model prediction and experimental data is seen to be reasonably good. In the cathode, the liquid volume fraction drops from the catalyst layer to the channel side, indicative of the direction for

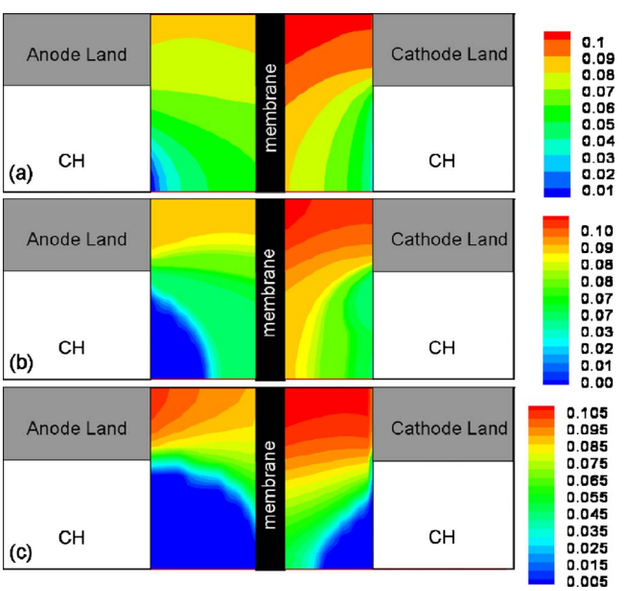

Figure 3. (Color online) The contours of the liquid water saturation at the operating condition of 0.75 A/cm^2, RHa/c = 100/100%, and (a) 40°C and 0.59 V, (b) 60°C and 0.65 V, and (c) 80°C and 0.67 V.

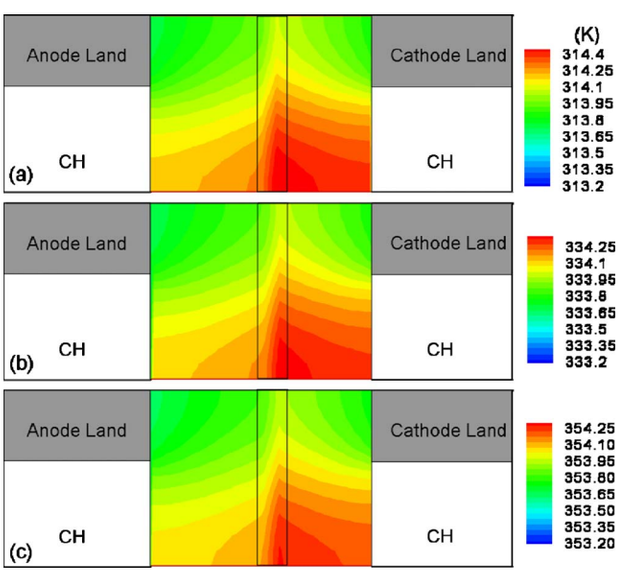

Figure 4. (Color online) The contours of temperature at the operating condition of 0.75 A/cm^2, RHa/c = 100/100%, and (a) 40°C and 0.59 V, (b) 60°C and 0.65 V, and (c) 80°C and 0.67 V.

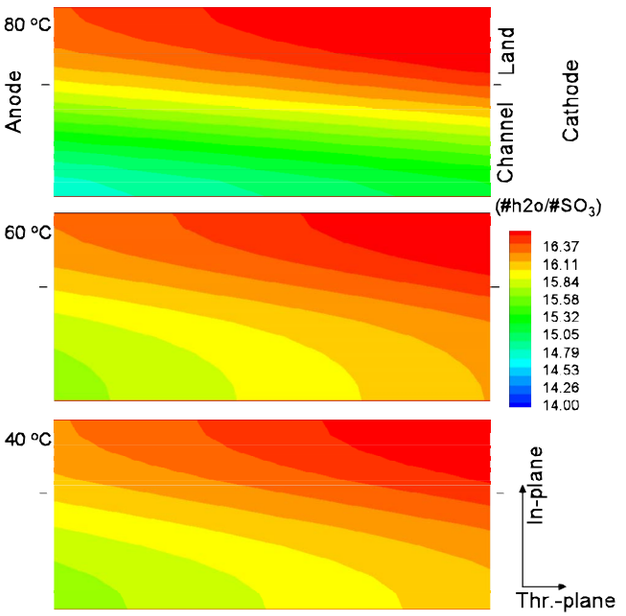

Figure 5. (Color online) Water content contours in the membrane at 0.75 A/cm^2 and RHa/c = 100/100%.

liquid drainage or water removal. The trends of water across the anode/cathode GDL and MEA can be readily explained by the detailed 2D water distributions shown in Fig. 3.

In order to provide a simple direct analysis on the through-plane water distribution in the cathode GDL, one can assume the capillary pressure as the only driving force for liquid movement. A 1D (the through-plane dimension or denoted as x here) analysis in the cathode can be performed to equate the capillary flux to the net liquid-water flux

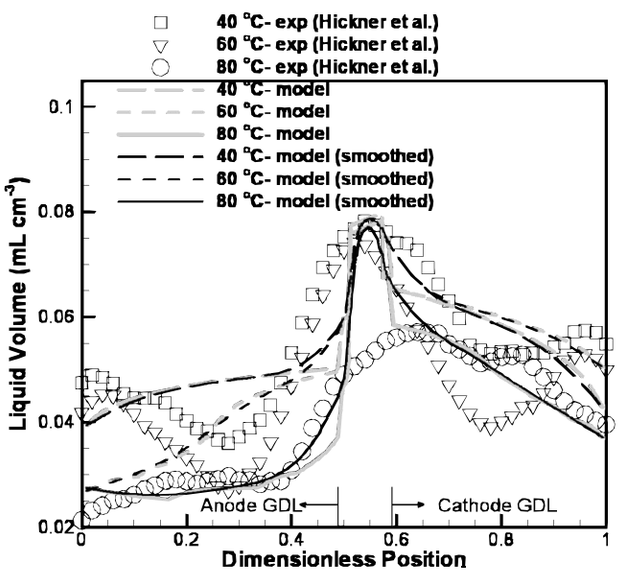

Figure 6. Comparison of water profiles in the MEA and GDLs from the model prediction and experimental data at 0.75 A/cm^2 and RHa/c = 100/100% (the experimental data are from Ref. 44).

$$\frac{k_r^{(l)} K}{\nu^{(l)}} \frac{dP_c}{dx} = \left(\frac{(1+2\alpha)}{2F} I - G_{\text{vapor}} \right) M_w \quad [34]$$

where G_{vapor} represents the portion taken away or added by the water-vapor diffusion. Furthermore, rewriting the above equation leads to

$$-D_c \frac{ds}{dx} = \left(\frac{(1+2\alpha)}{2F} I - G_{\text{vapor}} \right) M_w \quad [35]$$

where $D_c = -\sigma/\nu^{(\ell)} \cos(\theta_c)(K\varepsilon)^{1/2} k_r^{(l)} dJ(s)/ds$.[55] The above simple analysis indicates that the capillary action is similar to a diffusion process, with the "diffusion coefficient" as a function of the liquid saturation s. Note that a number of the factors, including current density I and water vapor-phase flux G_{vapor}, may affect the profile of the through-plane water content. For the 80°C case, more water can be transported via the vapor phase;[24,36] therefore G_{vapor} becomes larger (hence the right side becomes smaller) in the diffusive flux formula of Eq. 35, which may contribute to its lower cathode water profile observed in this figure.

In addition, similar analysis can be applied in the anode where the trend is slightly different with that in the cathode as shown in Fig. 6: at or near the anode channel/GDL interface (dimensionless position = 0), the liquid volume values for 60 and 80°C are about the same whereas that for 40°C is much higher. Figure 3 shows that a very small portion of anode GDL exhibits single phase at 40°C whereas a large portion for 60 and 80°C, which is the reason for the higher liquid volume for 40°C. However, the strong vapor phase diffusion in the anode at 80°C leads a high liquid saturation under the land as compared with 60°C, which may explain the comparable liquid volume values for these two temperatures.

In addition, protons may dissociate incompletely from the backbone, which can directly affect the water content in the membrane. Other factors such as membrane swelling, compression due to load, or force applied at the external wall surfaces may also affect water content in the membrane, as explained previously. In the present work, an α value of 0.15 was used and this value renders a reasonably good or satisfactory agreement on the water profile between the model prediction and the experimental data. Weber and Hickner[36] adopted a value of unity for α, which results in a much larger deviation ($>$ 300%) or factor of 4 difference[46] between their pseudo 2D (or 1 + 1D) prediction and experimental data. A value of α lower than unity is physically more plausible. We also use the same α value to compute water profile across the MEA–GDL and compare with the experimental data reported by Mukundan and Borup[45] and Borup[46] of LANL, and the comparison results are shown in Fig. 7. Here, we adopt the model geometry to match the LANL's experimental setup (e.g., the N117 membrane and GDL). It can be seen that our model prediction agrees reasonably well with their data at two different current densities. In addition, the LANL data show a similar trend on water profile to that from Hickner et al.,[44] particularly in the membrane.

It is worthy to mention that application of neutron imaging in fuel cell is relatively new and the probed curves are also affected by several uncertainties such as geometric blur in neutron imaging, detector resolution, fuel cell misalignment, and other mishandlings. Geometric blur is determined by several factors such as the distances between detector and object, h, and between detector and neutron source, L, and the size of the neutron beam source, d, (the geometric resolution = d $\times$ h/L; for an excellent discussion on this topic, see http://physics.nist.gov/MajResFac/NIF/geometric.html.) Misalignment might introduce a considerable error given the small thicknesses of the GDL and MEA, for an example, a misalignment of 1° (the angle Θ between the neutron beam and fuel cell MEA plane) will introduce an error of $\sim$350 μm ($\sim \sin\Theta \times$ Lp) given that the projected length Lp of the fuel cell is 2 cm. By comparing with the experimental data from the two separate, reputable groups using one set of model parameters, we can minimize the effect of uncertainties involved in neutron imaging on our model validation.

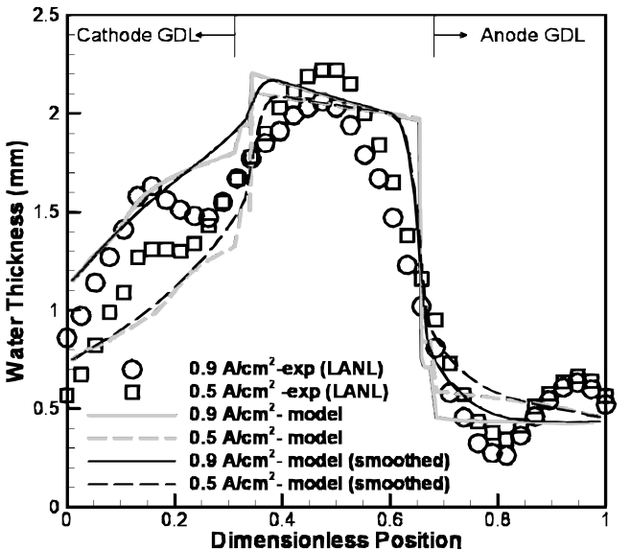

Figure 7. Comparison of the predicted water profiles and experimental data for RHa/c = 100/50% and 40°C [the experimental data are from LANL (Ref. 46)].

In addition, despite the reasonable good agreement we also admit that there exists discrepancy between the model prediction and neutron imaging data (at some location the error is close to 20%), which is likely due to the above mentioned uncertainties such as the "geometric blur" and detector resolution, and exclusion of MPLs and anisotropic properties of GDLs/membrane in the model. Moreover, discontinuities of water profiles at the MEA–GDL interface are shown in the model prediction, but not in the neutron imaging curves. A water depth discontinuity likely exists in a real fuel cell as membrane water concentration is several orders of magnitude higher than the gas phase. One possible reason of the smooth curves in neutron imaging data is the "geometric blur," which may "blur" or smooth the discontinuities. To approximate the effect of the "geometric blur," we applied the Gaussian blurring (or smoothing) technique[56,57] to the model prediction, as was done by Preston et al.[58] In this smoothing technique, a Gaussian kernel $g(\sigma,x) = 1/\sqrt{2\pi}\sigma e^{-x^2/2\sigma^2}$ is adopted to transform the value at a point (similar to a pixel in the neutron image) by the weighted average of itself and points in the neighborhood, i.e., $F(x) = \int_{-\infty}^{+\infty} f(x')g(\sigma,x' - x)dx'$, where σ is the standard deviation, x location, $f(x)$ the curve prior to smoothing, and $F(x)$ the smoothed curve. The smoothing process or detailed procedure adopted in the present work for a discrete set of points $\{f_i\}$ in the model prediction is as follow:

1. Create a new set of data $\{f_i\}$ at uniform gridpoints based on the linear interpolation of a model prediction;
2. Choose a Gaussian kernel (here we used a seven points discrete kernel[58] $\{g_m\}$ where m = −3, −2, −1, 0, 1, 2, 3);
3. Calculate a set of new data $\{F_i\}$ by using $F_i = \Sigma_m f_{i+m} g_m$;
4. Replace $\{f_i\}$ by $\{F_i\}$ and repeat Steps 1–3 till a sufficient degree of smoothing is achieved (in the present work five to ten repeats were carried out).

The final data set $\{F_i\}$ was then used to plot the smoothed curve, which was also shown in the figure. It can be seen that the discontinuities disappear, better matching the neutron imaging profiles. However, it is worthy to note that capturing such water discontinuity is important for understanding of the liquid-water behavior in a fuel cell. Hopefully, our present work will motivate the experimentalists to obtain more accurate data using neutron imaging, X-ray, or other techniques. We also hope that our present work will motivate modelers to develop higher fidelity models so as to more accurately predict water distribution.

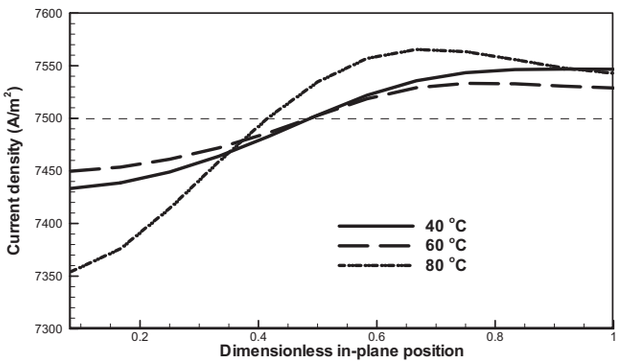

Figure 8. Predicted current density profiles for the three operating temperatures at 0.75 A/cm^2 and RHa/c = 100/100%.

Figure 8 displays the computed current density profiles for the three cell temperatures considered in the present work. As the average current density is set at 0.75 A/cm^2, variation of the local current is around this average value. Small variations are observed for the three cases with the largest one appearing at 80°C. Its explanation can be aided by Fig. 5: as this operation is controlled by the Ohmic resistance, the lower water content under the channel at 80°C leads to a higher Ohmic polarization, causing a relatively lower local reaction rate. However, the variation is small due to the membrane being highly hydrated for the three cases as shown in Fig. 5.

Figure 9 shows the current density variations at 40°C operating temperature and various RHs. At low RH, the membrane hydration levels may be quite different between the regions under the channel and land; consequently, the Ohmic resistance will differ greatly from location to location. This figure indicates that large current density variations take place for the two cases of dry anode (i.e., the anode RH is 50%). For the other cases where anode is fed with fully humidified gas, the degree of variation is small even for the case in which 50% RH is used in the cathode.

Figure 10 shows the detailed liquid-water distribution within the anode and cathode GDLs for the three dry cases. It can be seen that in the driest case (50% RH on both sides) liquid water still appears but the region is limited in a minute area under the land, while vast portion of the GDL (both anode and cathode) is subjected to dry operation. Comparing with the cases of 50% RH in the anode and cathode (the other side is 100% RH, i.e., RHa/c = 50/100% and 100/50%, respectively), the dry anode indicates a smaller wetted

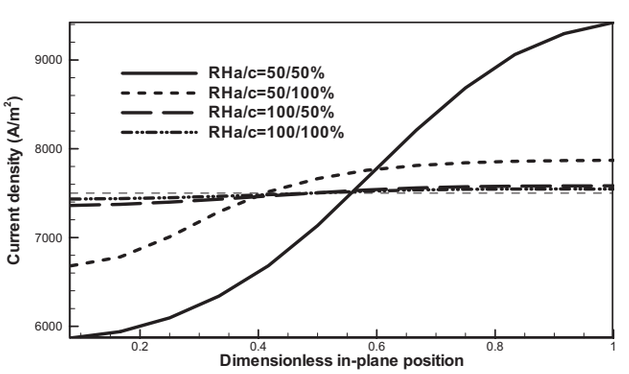

Figure 9. Predicted current density profiles for varying (RHs at 0.75 A/cm^2 and 40°C.

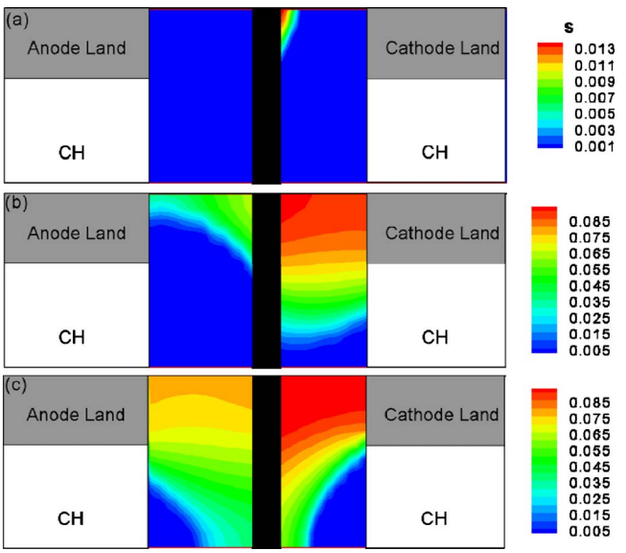

Figure 10. (Color online) Liquid water saturation distributions for varying RH at 0.75 A/cm^2 and 40°C: (a) RHa/c = 50/50% (0.51 V), (b) RHa/c = 50/100% (0.56 V), and (c) RHa/c = 100/50% (0.60 V).

region in the GDL, particularly in the anode side. For the case that only cathode is dry (i.e., RHa/c = 100/50%), all the region of the MEA is in the two-phase operation; consequently, a higher water content is secured in the membrane, leading to a small variation of the current density as shown in the previous figure.

Figure 11 shows the water profiles across the MEA–GDL for

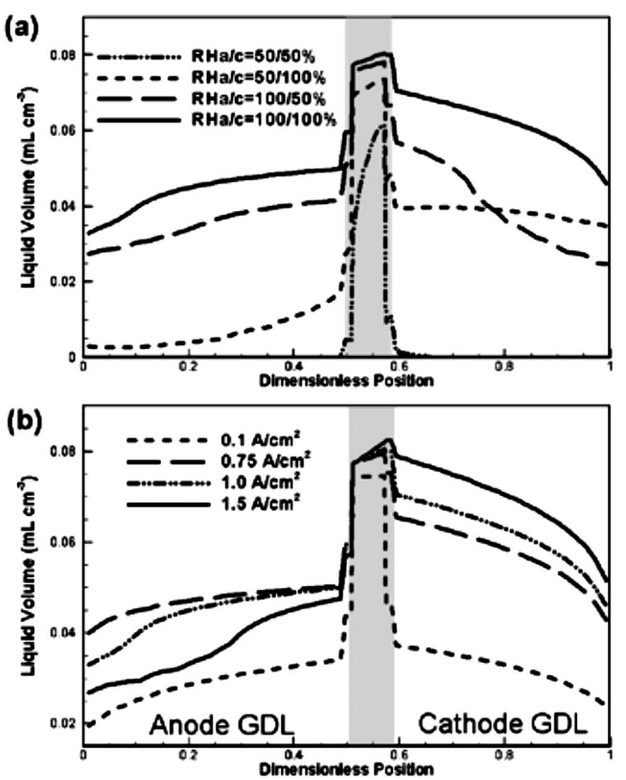

Figure 11. Liquid water profiles at 40°C operating temperature for (a) varying RH at 0.75 A/cm^2 and (b) different current densities at RHa/c = 100/100%.

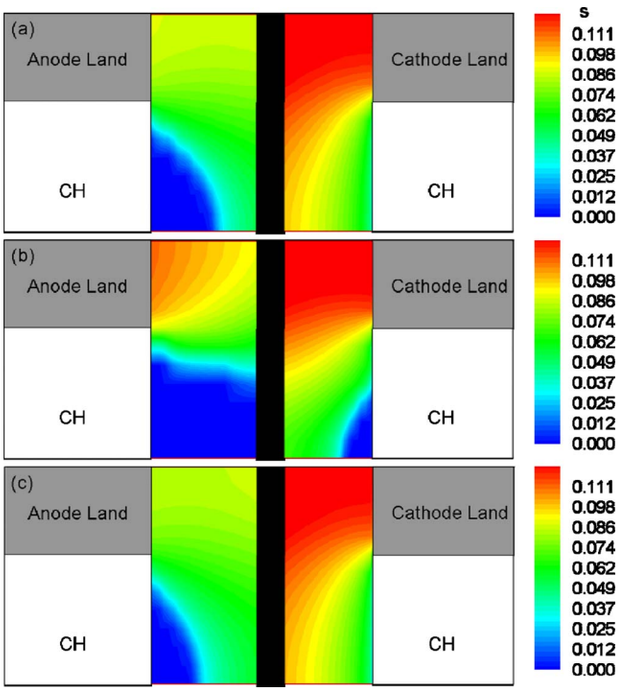

Figure 12. (Color online) Liquid water saturation contours in the GDL at 1.5 A/cm^2, RHa/c = 100/100%, and 40°C when using different GDL thermal conductivities: (a) 3.0 W/m K, (b) 1.0 W/m K, and (c) 6.0 W/m K.

various RHs (Fig. 11a) and current densities (Fig. 11b). It can be seen from Fig. 11a that the anode water content directly increases with the RH value in the anode whereas in the cathode side, part of the GDL for the case of RHa/c = 100/50% is even higher than that at 50/100%. Figure 11b displays the water-content profiles at various operating current densities for RHa/c = 100/100%. It can be seen that the cathode water-content profile increases with the current density; however, the anode side indicates a complex pattern: 0.75 A/cm^2 gives rise to the highest water content in the anode. Figure 12a shows the detailed 2D water saturation for the case of 1.5 A/cm^2 and RHa/c = 100/100%. It can be seen that the part of the anode GDL is free of liquid water which is due to the impact of the strong water electro-osmotic drag at high current density. Lastly, the thermal conductivity of GDL is also critical to liquid-water distribution within fuel cell. Figure 12b presents computed liquid saturation using parameters the same case as Fig. 12a but with a different thermal conductivity, namely, 1.0 W/m K. It can be seen that the liquid region is smaller than that shown in Fig. 12a where a GDL conductivity of 3.0 W/m K is used, particularly in the anode. This can also be explained by the stronger water vapor phase diffusion at lower GDL thermal conductivity which causes a larger temperature gradient. In addition, the vapor phase diffusion enhances the liquid level under the land,[24] which explains the higher water saturation under the land in this figure comparing with Fig. 12b. A larger GDL thermal conductivity will depress the vapor phase diffusion. Figure 12c shows such a case with the GDL conductivity doubling that of Fig. 12a and indicates a larger two-phase region in the anode. Similar trend between the two-phase region and thermal conductivity was also indicated from the neutron imaging results of Kandlikar et al.[59]

Conclusions

A multidimensional model was developed and employed to elucidate the water distribution across the MEA–GDL component in a PEFC. The present model is based on the conservations of mass, momentum, species (including liquid water), energy, and charges.

2D simulation results were computed using the model. We found that liquid-water content may be lower at higher cell temperatures due to greater water evaporation and stronger water diffusion in vapor phase. At 40°C operation where water diffusion in vapor phase is relatively weak, the liquid-water content was found to increase monotonically with current density in the cathode GDL but a complex trend was observed in the anode. It was also found that changing the RHs in the anode and cathode profoundly affects the liquid-water profile in the PEFC. Moreover, reducing the GDL thermal conductivity may shrink the size of two-phase region in the PEFC. Results from the present study also show that 2D (through- plus in-plane dimension) fuel cell simulation is required to be able to predict the water distribution across the MEA–GDL. Lastly, predictions computed from the present model were compared with the neutron-imaging data reported by two separate groups in terms of the water through-plane profiles and reasonably good agreement was obtained. Qualitative comparison with neutron imaging data from a third group was also made and good agreement was achieved.

Acknowledgments

Funding support of this work was provided by Sandia National Laboratories. Sandia is a multiprogram laboratory operated by Sandia Corporation, a Lockheed Martin Company for the United States Department of Energy's National Nuclear Security Administration under contract no. DE-AC04-94AL85000.

Sandia National Laboratories assisted in meeting the publication costs of this article.

List of Symbols

C	molar concentration, mol/m^3
D	mass diffusivity of species, m^2/s
F	Faraday's constant, 96 487 C/equivalent
$\vec{G}$	species diffusion/permeation flux, mol m^{-2}
I	current density, A/cm^2
$\vec{i}$	superficial current density, A cm^{-2}
j	transfer current density, A cm^{-3}
$\vec{j}^{(l)}$	mass flux of liquid phase, kg m^{-2} s^{-1}
K	permeability, m^2
k_r	relative permeability
M	molecular weight, kg/mol
P	pressure, Pa
R	gas constant, 8.134 J/mol K
s	liquid saturation
S	source term in transport equations
T	temperature, K
U_o	equilibrium potential, V
$\vec{u}$	velocity vector, m/s

Greek

α	water concentration correction factor
γ_c	correction factor for species convection
ε	porosity
η	surface overpotential, V
λ	membrane water content
$\lambda^{(k)}$	mobility of phase k
ν	kinematic viscosity, m^2/s
ρ	density, kg/m^3
σ	surface tension, N/m
$\vec{\tau}$	shear stress, N m^{-2} Φ phase potential, V

Superscripts and Subscripts

a	anode
c	cathode
d	electro-osmotic drag
eff	effective value
g	gas phase
k	species; liquid or gas phase
l	liquid
m	membrane
o	reference value
perm	permeation
sat	saturate value
s	liquid saturation or solid phase

References

1. C. Y. Wang, *Chem. Rev. (Washington, D.C.)*, **104**, 4727 (2004).
2. A. Z. Weber and J. Newman, *Chem. Rev. (Washington, D.C.)*, **104**, 4679 (2004).
3. T. E. Springer, T. A. Zawodzinski, and S. Gottesfeld, *J. Electrochem. Soc.*, **138**, 2334 (1991).
4. D. M. Bernardi, and M. W. Verbrugge, *J. Electrochem. Soc.*, **139**, 2477 (1992).
5. A. Rowe and X. Li, *J. Power Sources*, **102**, 82 (2001).
6. T. V. Nguyen and R. E. White, *J. Electrochem. Soc.*, **140**, 2178 (1993).
7. V. Gurau, H. Liu, and S. Kakac, *AIChE J.*, **44**, 2410 (1998).
8. S. Um, C.-Y. Wang, and K. S. Chen, *J. Electrochem. Soc.*, **147**, 4485 (2000).
9. W. He, J. S. Yi, and T. V. Nguyen, *AIChE J.*, **46**, 2053 (2000).
10. Z. H. Wang, C. Y. Wang, and K. S. Chen, *J. Power Sources*, **94**, 40 (2001).
11. D. Natarajan and T. V. Nguyen, *J. Electrochem. Soc.*, **148**, A1324 (2001).
12. L. You and H. Liu, *Int. J. Heat Mass Transfer*, **45**, 2277 (2002).
13. A. Z. Weber, R. M. Darling, and J. Newman, *J. Electrochem. Soc.*, **151**, 1715 (2004).
14. U. Pasaogullari and C. Y. Wang, *J. Electrochem. Soc.*, **151**, 399 (2004).
15. U. Pasaogullari and C. Y. Wang, *Electrochim. Acta*, **49**, 4359 (2004).
16. C. Ziegler, H. M. Yu, and J. O. Schumacher, *J. Electrochem. Soc.*, **152**, A1555 (2005).
17. H. Sun, H. Liu, and L.-J. Guo, *J. Power Sources*, **143**, 125 (2005).
18. H. Meng and C. Y. Wang, *J. Electrochem. Soc.*, **152**, 1733 (2005).
19. J.-H. Nam and M. Kaviany, *Int. J. Heat Mass Transfer*, **46**, 4595 (2003).
20. J. Yuan and B. Sunden, *Electrochim. Acta*, **50**, 677 (2004).
21. T. Berning and N. Djlali, *J. Electrochem. Soc.*, **150**, A1589 (2003).
22. S. Mazumder and J. V. Cole, *J. Electrochem. Soc.*, **150**, 1510 (2003).
23. E. Birgersson, M. Noponen, and M. Vynnycky, *J. Electrochem. Soc.*, **152**, A1021 (2005).
24. Y. Wang and C. Y. Wang, *J. Electrochem. Soc.*, **153**, A1193 (2006).
25. A. Z. Weber and J. Newman, *J. Electrochem. Soc.*, **153**, A2205 (2006).
26. G. Luo, H. Ju, and C. Y. Wang, *J. Electrochem. Soc.*, **154**, B316 (2007).
27. Y. Wang, *J. Power Sources*, **185**, 261 (2008).
28. Y. Wang, S. Basu, and C. Y. Wang, *J. Power Sources*, **179**, 603 (2008).
29. Y. Wang, *J. Electrochem. Soc.*, **156**, B1134 (2009).
30. Y. Wang, C. Y. Wang, and K. S. Chen, *Electrochim. Acta*, **52**, 3965 (2007).
31. S. Basu, C.-Y. Wang, and K. S. Chen, *J. Electrochem. Soc.*, **156**, B748 (2009).
32. P. P. Mukherjee and C. Y. Wang, *J. Electrochem. Soc.*, **154**, B1121 (2007).
33. P. P. Mukherjee, C.-Y. Wang, and Q. Kang, *Electrochim. Acta*, **54**, 6861 (2009).
34. J. Li, C. Y. Wang, and A. Su, *J. Electrochem. Soc.*, **155**, B64 (2008).
35. H. Ju and C. Y. Wang, *J. Electrochem. Soc.*, **151**, A1954 (2004).
36. A. Z. Weber and M. A. Hickner, *Electrochim. Acta*, **53**, 7668 (2008).
37. R. Satija, D. L. Jacobson, M. Arif, and S. A. Werner, *J. Power Sources*, **129**, 238 (2004).
38. T. A. Trabold, J. P. Owejan, D. L. Jacobson, M. Arif, and P. R. Huffman, *Int. J. Heat Mass Transfer*, **49**, 4712 (2006).
39. J. P. Owejan, T. A. Trabold, D. L. Jacobson, D. R. Baker, D. S. Hussey, and M. Arif, *Int. J. Heat Mass Transfer*, **49**, 4721 (2006).
40. M. A. Hickner, N. P. Siegel, K. S. Chen, D. N. McBrayer, D. S. Hussey, D. L. Jacobson, and M. Arif, *J. Electrochem. Soc.*, **153**, A902 (2006).
41. J. P. Owejan, T. A. Trabold, D. L. Jacobson, M. Arif, and S. G. Kandlikar, *Int. J. Hydrogen Energy*, **32**, 4489 (2007).
42. M. A. Hickner, N. P. Siegel, K. S. Chen, D. S. Hussey, D. L. Jacobson, and M. Arif, *J. Electrochem. Soc.*, **155**, B294 (2008).
43. D. S. Hussey, D. L. Jacobson, M. Arif, J. P. Owejan, J. J. Gagliardo, and T. A. Trabold, *J. Power Sources*, **172**, 225 (2007).
44. M. A. Hickner, N. P. Siegel, K. S. Chen, D. S. Hussey, D. L. Jacobson, and M. Arif, *J. Electrochem. Soc.*, **155**, B427 (2008).
45. R. Mukundan and R. L. Borup, *Fuel Cells*, **9**, 499 (2009).
46. R. Borup, Water Transport Exploratory Studies, DOE Hydrogen Program Review, May 18–22, 2009.
47. S. Tsushima, K. Teranishi, and S. Hirai, *Electrochem. Solid-State Lett.*, **7**, A269 (2004).
48. P. K. Sinha, P. Halleck, and C.-Y. Wang, *Electrochem. Solid-State Lett.*, **9**, A344 (2006).
49. C. Y. Wang and P. Cheng, in *Advances in Heat Transfer*, Vol. 30, J. P. Hartnett Jr., et al., Editors, p. 93, Academic, New York (1997).
50. J. D. Fairweather, P. Cheung, J. StPierre and D. T. Schwartz, *Electrochem. Commun.*, **9**, 2340 (2007).
51. J. T. Gostick, M. A. Ioannidis, M. W. Fowler, and M. D. Pritzker, *Electrochem. Commun.*, **10**, 1520 (2008).
52. K. G. Gallagher, R. M. Darling, T. W. Patterson, and M. L. Perry, *J. Electrochem. Soc.*, **155**, B1225 (2008).
53. T. A. Zawodzinski, J. Davey, J. Valerio, and S. Gottesfeld, *Electrochim. Acta*, **40**, 297 (1995).
54. S. Motupally, A. J. Becker, and J. W. Weidner, *J. Electrochem. Soc.*, **147**, 3171 (2000).
55. Y. Wang and X. Feng, *J. Electrochem. Soc.*, **155**, B1289 (2008).
56. R. Andonie and E. Carai, *Computers and Artificial Intelligence*, **11**, 363 (1992).
57. B. S. Moon, *Korean J. Comput. Appl. Math.*, **8**, 507 (2001).
58. J. S. Preston, R. S. Fu, U. Pasaogullari, D. S. Hussey, and D. L. Jacobson, *ECS Trans.*, **25**(1), 311 (2009).
59. S. Kandlikar, Z. Lu, T. Trabold, J. Owejan, J. Gagliardo, J. Allen, and R. Shahbazian-Yassar, Visualization of Fuel Cell Water Transport and Performance Characterization Under Freezing Conditions, DOE Hydrogen Program Review, May 18–22, 2009.